agriculture

MDPI

Article

Calibration of DEM Polyhedron Model for Wheat Seed Based on Angle of Repose Test and Semi-Resolved CFD-DEM Coupling Simulation

Longbao Wang [1,2], Hanyu Yang [1,2], Zhinan Wang [1,2], Qingjie Wang [1,2], Caiyun Lu [1,2], Chao Wang [1,2] and Jin He [1,2,*]

[1] College of Engineering, China Agricultural University, Beijing 100083, China; bs20233070709@cau.edu.cn (L.W.); s20213071335@cau.edu.cn (H.Y.); zhinan.wang@cau.edu.cn (Z.W.); wangqingjie@cau.edu.cn (Q.W.); lucaiyun@cau.edu.cn (C.L.); superc@cau.edu.cn (C.W.)
[2] Key Laboratory of Agricultural Equipment for Conservation Tillage, Ministry of Agriculture and Rural Affairs, Beijing 100083, China
* Correspondence: hejin@cau.edu.cn; Tel.: +86-010-6273-7300

Abstract: The shape of particles is a critical determinant that significantly influences the accuracy of discrete element simulations. To reduce the discrepancies between the discrete element model of wheat seeds and the actual particle shapes, and to enhance the accuracy of Computational Fluid Dynamics-Discrete Element Method (CFD-DEM) coupling simulations in gas–solid two-phase flow studies, We employed laser scanning and inverse modeling techniques to develop a three-dimensional (3D) reconstruction of the wheat seed. Subsequently, we employed Rocky DEM simulation software to develop a polyhedron model and an Angle of Repose (AOR) test model. The interval range of material parameters was determined through a series of physical experiments and subsequently employed to delineate the high and low levels of parameters for the simulation tests. The simulation parameters were calibrated using data from AOR simulation tests. The Plackett–Burman test, Steepest-Ascent test, and Box–Behnken test were conducted sequentially to determine the optimal parameter configuration. A test bench for wheat gas-assisted seeding was constructed, and a semi-resolved CFD-DEM coupling simulation model was developed to perform comparative analysis. The results demonstrated that the optimal parameters were as follows: the static friction coefficient of wheat seed was 0.15, the dynamic friction coefficient of wheat seed was 0.11694, and the dynamic friction coefficient between wheat seed and resin was 0.0797. In this scenario, the relative error of AOR was 2.3% and the maximum relative error of ejection velocity observed was 4.1%. The reliability of the polyhedron model and its calibration parameters was rigorously validated, thereby providing a robust reference for studies on gas–solid two-phase flows.

Keywords: wheat seed; polyhedron; angle of repose; DEM; calibration; semi-resolved CFD-DEM

check for updates

Academic Editor: Fengwei Gu

Received: 12 January 2025
Revised: 21 February 2025
Accepted: 24 February 2025
Published: 26 February 2025
Corrected: 9 July 2025

Citation: Wang, L.; Yang, H.; Wang, Z.; Wang, Q.; Lu, C.; Wang, C.; He, J. Calibration of DEM Polyhedron Model for Wheat Seed Based on Angle of Repose Test and Semi-Resolved CFD-DEM Coupling Simulation. *Agriculture* **2025**, *15*, 506. https://doi.org/10.3390/agriculture15050506

Copyright: © 2025 by the authors. Licensee MDPI, Basel, Switzerland. This article is an open access article distributed under the terms and conditions of the Creative Commons Attribution (CC BY) license (https://creativecommons.org/licenses/by/4.0/).

1. Introduction

The Discrete Element Method (DEM) is extensively utilized in the field of wheat seeding research [1]. In this study, a discrete element simulation model is developed to simulate the wheat seeding process, thereby providing a valuable reference for the optimization and design of seed-metering device. Discrete element simulation parameters primarily encompass material-intrinsic and contact parameters [2]. The intrinsic parameters are the inherent characteristics of the material that can be directly quantified through physical experiment.

Contact parameters, on the other hand, represent the physical properties at the interface between materials and require calibration via a combination of physical experiment and simulation [3]. The contact parameters are typically calibrated through AOR tests [4]. The AOR serves as a critical parameter for characterizing flow characteristics [5]. In recent years, the application of 3D printing technology in construction of seed-metering device has gained prominence, with resin materials being increasingly utilized [6]. Consequently, this study aims to calibrate the contact parameters between wheat seeds and resin materials.

Numerous scholars have conducted extensive research on wheat seed calibration. Liu et al. [7,8] calibrated the contact parameters through AOR tests and response surface optimization methods, subsequently constructing a viscoelastic–plastic contact model. Zhang et al. [9] conducted AOR tests to calibrate the contact parameters between wheat seeds and grinding rollers following wheat moistening. Wang et al. [10] calibrated the contact parameters through AOR and uniaxial compression tests. Sugirbay et al. [11] calibrated the contact parameters by conducting rotational drum tests. Horabik et al. [12] calibrated the parameters of the contact model using data from load-to-unload cycle tests. Discrete element simulation parameter calibration has evolved into a standardized procedure. When the focus of research is on particle flow dynamics, the characteristics of particle crushing may be disregarded. Under these circumstances, the parameter calibration methodology typically emphasizes the repose angle test. Petingco et al. [13] developed single-sphere and five-sphere models to investigate the impact of particle fall height and size distribution on wheat bulk density. Zhou et al. [14], Chen et al. [15] and Ma et al. [16] utilized scanning technology to construct 3D models and develop a multi-sphere model. Lu et al. [17] developed an ellipsoid model and validated its feasibility by comparing it with the multi-sphere model. Sun et al. [18] and Fan et al. [19] developed a comprehensive multi-domain modeling approach. The aforementioned studies utilized multi-spherical or ellipsoidal models to approximate non-spherical particles [20,21]. These modeling approaches appropriately simplify the characteristics of the grains but do not account for the irregular shapes of wheat seeds. However, the multi-sphere model requires manual or software-based arrangement and combination of the filled spheres, which may result in discrepancies between the particle centroid positions and actual conditions. Theoretically, a higher number of filled spheres increases modeling accuracy. This introduces multiple contact points among particles, significantly reducing computational efficiency. The ellipsoid model inadequately represents the shape of wheat seed grooves and neglects the multipoint contact and collision mechanics of grains. In contrast, the polyhedron model can be developed with a high aspect ratio and sharp edges by assembling triangular surface elements into particulate structures. This modeling approach eliminates the need for particle filling, thereby providing a more accurate representation of real-world conditions. Additionally, it facilitates customized modeling of irregular non-spherical particles.

The shape of wheat seeds exhibits irregularity, with variations in the dimensions of the three principal axes. Owing to the limitations inherent in the multi-spherical and ellipsoidal model, the shape and dimensions of the simulated particles exhibit discrepancies when compared to those of actual particles [22]. The shape and dimensions of particles have a substantial impact on the accuracy of simulations, particularly in CFD-DEM coupling simulations [23,24]. Hence, enhancing the accuracy of wheat seed modeling is critically important to provide a robust reference for studies on precision vacuum seeding, fluid drying, centralized pneumatic seeding, and optimization of design of the structural configuration for grain threshing machinery [25–33].

Therefore, the objectives of this study were to the following: (1) Develop a DEM polyhedron model for wheat seed to enhance modeling accuracy. (2) Calibration of simulation parameters via physical experiments and AOR simulation tests. (3) Development of a

semi-resolved CFD-DEM coupling simulation model to investigate the process of airflow-assisted seeding of wheat seeds. Ultimately, the simulation parameters were validated through bench test data from airflow-assisted seeding experiments. (4) Provide a robust reference and support for the study of gas–solid two-phase flow of wheat seeds.

2. Materials and Methods

2.1. Test Material Characteristics

Lu Yuan No. 502 (LY502) wheat seed was selected as the research subject in this study. This variety has been officially endorsed for promotion for over five years. It has consistently ranked among the top ten in terms of suitable sowing area for three consecutive years and has been included in the "National Catalogue of Promoted Excellent Crop Varieties (2023)" by the Seed Industry Management Department of the Ministry of Agriculture and Rural Affairs of China. The selected wall material was resin, which is a crucial material in the 3D printing process. Resin is the material of which many laboratory assets used in the calibration procedures were made, thus was essential when replicating these experiments in the DEM environment.

2.2. Size Analysis and Modelling of Wheat Seed Particles

Wheat seeds exhibit irregular shape characteristics, and their geometric properties are typically quantified using triaxial dimensions [34]. A digital display Vernier caliper with an accuracy of 0.01 mm was employed to measure the triaxial dimensions of 100 randomly selected wheat seeds. As illustrated in Figure 1, the length (L), width (W), and thickness (T) of each wheat seed were measured individually. Figure 2 illustrates the fitted curve representing the normal distribution of triaxial size. To accurately establish discrete metamodels of wheat seeds, specimens with triaxial dimensions approximating the average were selected. We employed 3D scanning technology to capture the external contours of wheat seeds (as illustrated in Figure 3b). This process precisely captures the 3D coordinates of the external surface of seeds, generating point cloud data (as illustrated in Figure 3c). Finally, the refined point cloud data were imported into post-processing software, where sharp and noisy points were eliminated to generate a precise three-dimensional model of the wheat seed (as illustrated in Figure 3d). The resulting STL files were subsequently imported into Rocky DEM 2024R1 software for the creation of a polyhedron model. Figure 3 illustrates the detailed procedure.

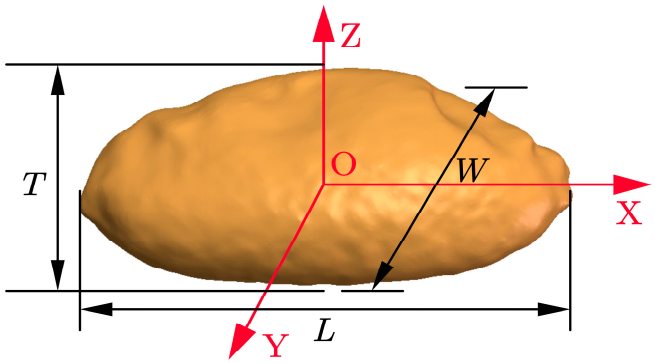
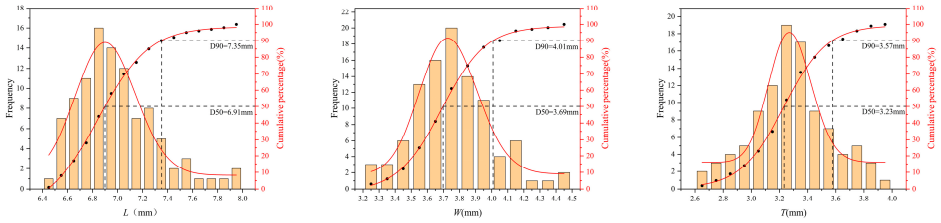


Figure 1. Triaxial size measurement position.



(**a**) Length distribution (**b**) Width distribution (**c**) Thickness distribution

Figure 2. Triaxial size distribution of LY502 wheat seed particles.

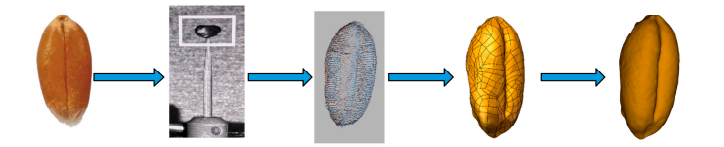


Figure 3. Construction process of wheat seed discrete element model.

2.3. Physical Experiments for the Calibration of Intrinsic Parameters

2.3.1. Young's Modulus and Poisson's Ratio

The Poisson's ratio and Young's modulus of the tested wheat seeds were determined through uniaxial compression tests conducted using a texture analyzer (model: TMS-Touch), as illustrated in Figure 4. The seeds were positioned horizontally on a flat surface and subjected to loading along the thickness direction via a circular probe. Post-processing of the uniaxial compression load–displacement data was performed, and the deformation of the seeds in both the length and thickness directions was measured using a digital Vernier caliper. Equations (1) and (2) were employed to calculate Young's modulus and Poisson's ratio, respectively [35]. The extreme values were obtained by conducting ten replicate tests.

$$E = \frac{\sigma}{\varepsilon} \tag{1}$$

where E is the Young's modulus of wheat seeds (Pa); σ is the maximum stress (Pa); ε is the linear deformation.

$$\nu = \frac{\Delta L / L}{\Delta T / T} \tag{2}$$

where ν is the Poisson's ratio of wheat seeds; ΔL is the deformation in the longitudinal direction of the seed (mm); L is the seed length along the original longitudinal direction (mm); ΔT is the deformation in the thickness direction of the seed (mm); T is the original length in the thickness direction of the seed (mm).

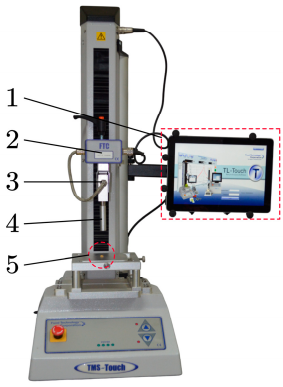


Figure 4. TMS-Touch texture analyzer: 1. control interface; 2. loadcell slider; 3. mechanical transducer; 4. metallic probe; 5. wheat seed.

2.3.2. Bulk Density

The bulk density of wheat seeds was determined using an intelligent powder characteristic tester (Model: Baxter BT-1001, manufactured by Dandong Baxter Instrument Co., Ltd., Dandong, China). As illustrated in Figure 5, during the experiment, wheat seeds were loaded into a calibrated standard container of fixed volume. Following this, the upper surface of the container was leveled off. Subsequently, the mass was measured, and the instrument automatically calculated the bulk density using Equation (3). We conducted this procedure ten times to ascertain the range of values derived from the test.

$$\rho_b = \frac{M_1 - M_0}{V} \tag{3}$$

where ρ_b is the bulk density (g/cm^3); M_1 is the total mass of seeds and conventional cylindrical container (g); M_0 is the mass of conventional cylindrical container (g); V is the capacity of conventional cylindrical container (cm^3).

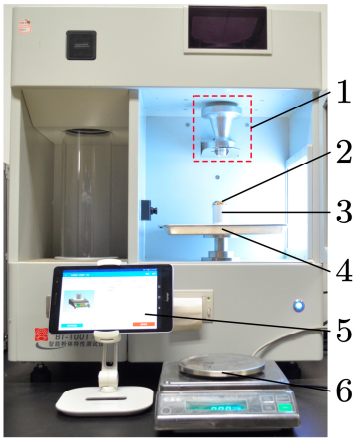


Figure 5. Bulk density measurement: 1. the hopper; 2. wheat seeds; 3. conventional cylindrical container; 4. the tray; 5. control interface; 6. electronic weighing scale.

2.4. Physical Experiments for the Calibration of Contact Parameters

2.4.1. Determination of the Friction Coefficient

As illustrated in Figure 6, the dynamic and static friction coefficients of wheat seed were measured using a coefficient of friction testing instrument (Model: MXD-01, Jinan SaiCheng Electronic Technology Co., Ltd., Jinan, China). The measurement principle involves fitting and placing the material to be tested on the instrument's surface. By determining the critical force required for relative displacement of the materials, which is equal to the product of the friction coefficient and the normal force, the instrument automatically calculates the dynamic and static friction coefficients. During the experiment, wheat seeds were securely fastened to the instrument's test platform, with an appropriate quantity of wheat seeds adhered to the test slider. The slider movement speed was set at 100 mm/min. Upon initiating the test, the slider traversed a predetermined distance, and the system automatically computed the dynamic or static friction coefficient between wheat particles. This procedure was replicated ten times to determine the extreme values. The dynamic and static friction coefficients between wheat seed and resin were determined following the same methodology.

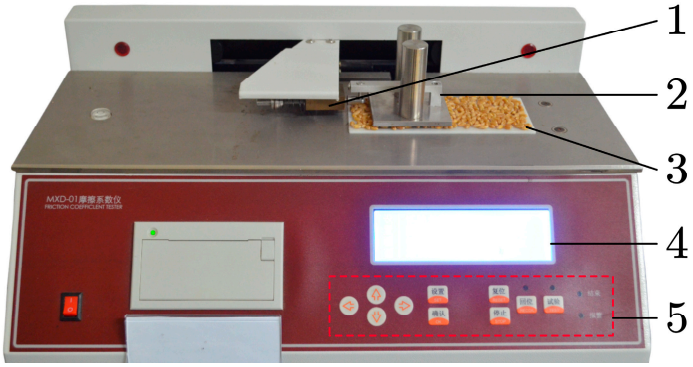


Figure 6. Determination of the friction coefficient: 1. mechanical transducer; 2. sliding block mechanism; 3. seed plate; 4. liquid crystal display panel; 5. operational control panel.

2.4.2. Determination of the Collision Restitution Coefficient

The collision restitution coefficient between wheat seed and resin was determined using the free-fall method for wheat seeds. The motion trajectory and data were recorded using a high-speed camera (model: 5KF-20, Hefei ZhongKe Junda Vision Co., Ltd., Hefei, China), as illustrated in Figure 7. During the experiment, wheat seeds were held with tweezers and raised to a fixed height H_0. The orientation of the seed was adjusted to ensure that upon release, the free fall would result in a collision with the resin material. The rebound height H_1 was measured using the high-speed camera and coordinate paper. The collision restitution coefficient between wheat seed and resin was calculated according to Equation (4), and the range of value was obtained by repeating the test ten times. The collision restitution coefficient of the wheat seed was also calculated using the same methodology.

$$e = \sqrt{\frac{H_1}{H_0}} \tag{4}$$

where e is the collision restitution coefficient; H_0 is the free-fall height of seeds (mm); H_1 is the seed rebound height measurement (mm).

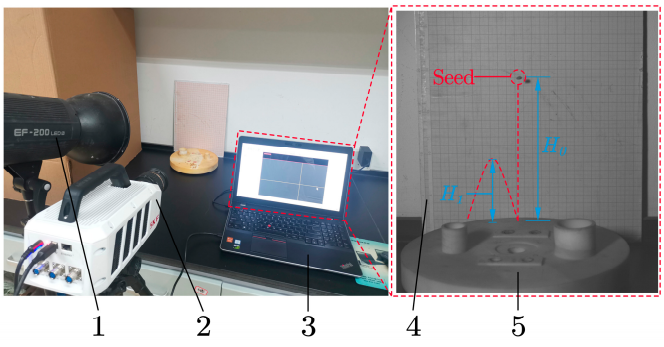


Figure 7. Determination of the collision restitution coefficient: 1. supplemental lighting; 2. high-speed camera; 3. portable computer; 4. graph paper; 5. resin plate.

2.5. Physical Experiments for Calibration of AOR

The AOR was measured using an intelligent powder characteristic tester (Model: BT-1001, Dandong Baxter Instrument Co., Ltd.). During the measurement process, wheat seeds were allowed to freely fall from a hopper and accumulate on a resin circular plate, forming an approximately conical pile. As illustrated in Figure 8, the instrument performs binary processing on the original image of the pile, extracts the edge contour via edge detection, and applies linear regression to the edge points of the contour curve. The angle between the fitted line and the horizontal plane is defined as the AOR. The test was conducted ten

times, and the resulting mean value was 32.9°. For the calibration test, the mean value was utilized as a parameter to adjust the optimization target.



(**a**) AOR test (**b**) The original image (**c**) Binarized image contour extraction

Figure 8. The procedure for determining the angle of repose: 1. the hopper; 2. ambient illumination source; 3. camera device; 4. wheat seeds; 5. resin plate; 6. the tray.

2.6. Modeling in Rocky DEM Software

2.6.1. Simulation Software and Contact Model

Rocky DEM 2024R1 was used to perform the DEM simulations. The normal force contact model was configured as the Hertzian Spring–Dashpot model, while the alternative tangential force contact model was designated as the Mindlin–Deresiewicz model.

The Hertzian Spring–Dashpot model bears resemblance to the Linear Spring–Dashpot model, with the primary distinction being that both the elastic and damping components of the normal force in the Hertzian model are nonlinear functions of the overlap [36]. The elastic component is grounded in the classical contact theory formulated by Hertz in the late nineteenth century [37]. The formulation of the Hertzian Spring–Dashpot model as implemented in Rocky DEM can be expressed as follows [38]:

$$F_n = \hat{K}_H s_n^{\frac{3}{2}} + \hat{C}_H s_n^{\frac{1}{4}} \dot{s}_n \tag{5}$$

where F_n is the normal elastic–plastic contact forces; s_n is the normal overlap value; $\dot{s}_n$ is the time derivative of the normal overlap; $\hat{C}_H$ is the damping coefficient. The stiffness coefficient $\hat{K}_H$ is defined as follows:

$$\hat{K}_H = \frac{4}{3} E^* \sqrt{R^*} \tag{6}$$

where E^* represents the reduced Young's modulus, which is defined by the following expression (7); R^* represents the effective or equivalent radius, which is defined by the following expression (8).

$$\frac{1}{E^*} = \frac{1-\nu_1^2}{E_1} + \frac{1-\nu_2^2}{E_2} \tag{7}$$

where E_1 and E_2 represent the Young's moduli of the two contacting particles or the particle and the boundary, contingent upon the type of contact. Additionally, ν_1 and ν_2 denote the respective Poisson's ratios

$$\frac{1}{R^*} = \begin{cases} \frac{2}{R_1} + \frac{2}{R_2} & (\text{for particle} - \text{particle collision}) \\ \frac{2}{R} & (\text{for particle} - \text{boundary collision}) \end{cases} \tag{8}$$

where R_1 and R_2 represent the dimensions of the particles involved in a particle–particle collision, while R denotes the dimension of the particle in a particle–boundary collision.

In accordance with the methodology initially proposed by Tsuji et al. [39], the damping coefficient for the Hertzian model in Rocky DEM is defined in a manner analogous to that of the linear spring–dashpot model:

$$\hat{C}_H = 2\eta_H \sqrt{m^* \hat{K}_H} \tag{9}$$

where m^* denotes the effective mass as previously defined in Equation (10), and η_H represents the damping ratio for the Hertzian Spring–Dashpot model. Antypov and Elliott [40] demonstrated that, through the application of appropriate variable transformations, the solution to a motion equation based on the Hertzian model can be mapped onto the solution of an equivalent equation derived from the linear spring–dashpot model. This equivalence is only possible if the damping coefficient for the Hertzian model is defined in Equation (11).

$$\frac{1}{m^*} = \begin{cases} \frac{1}{m_1} + \frac{1}{m_2} & (\text{for particle} - \text{particle collision}) \\ \frac{1}{m} & (\text{for particle} - \text{boundary collision}) \end{cases} \tag{10}$$

where m_1 and m_2 denote the masses of the interacting particles, while m represents the mass of the particle in contact with the boundary.

$$\eta_H = \frac{\sqrt{5}}{2}\eta \tag{11}$$

where η represents the damping ratio, consistent with that utilized in the linear spring–dashpot model. In Rocky DEM, the value of η is determined by solving Equation (12) [41], and subsequently, this value is employed in Equation (11) to derive η_H. This approach ensures that, irrespective of whether the linear spring–dashpot or Hertzian model is applied, the viscous energy dissipation during a collision event remains equivalent to the specified value through the coefficient of restitution.

$$e = \begin{cases} \exp\left[-\frac{\eta}{\sqrt{1-\eta^2}}\left(\pi - \arctan\frac{2\eta\sqrt{1-\eta^2}}{1-\eta^2}\right)\right] & \text{if } 0 \le \eta \le \frac{1}{\sqrt{2}} \\ \exp\left(-\frac{\eta}{\sqrt{1-\eta^2}}\arctan\frac{2\eta\sqrt{1-\eta^2}}{1-\eta^2}\right) & \text{if } \frac{1}{\sqrt{2}} \le \eta \le 1 \\ \exp\left(-\frac{\eta}{\sqrt{\eta^2-1}}\ln\frac{\eta+\sqrt{\eta^2-1}}{\eta-\sqrt{\eta^2-1}}\right) & \text{if } \eta > 1 \end{cases} \tag{12}$$

The tangential force in the Mindlin–Deresiewicz model is described by the following expressions [42]:

$$F_\tau = -\mu F_n\left(1 - \zeta^{\frac{3}{2}}\right)\frac{s_\tau}{|s_\tau|} + \eta_\tau\sqrt{\frac{6\mu m^* F_n}{s_{\tau,max}}}\zeta^{\frac{1}{4}}\dot{s}_\tau \tag{13}$$

$$\zeta = 1 - \frac{\min(|s_\tau|, s_{\tau,max})}{s_{\tau,max}} \tag{14}$$

where μ is the friction coefficient, as defined in Equation (15); s_τ represents the tangential relative displacement at the contact interface; $\dot{s}_\tau$ represents the tangential component of the relative velocity at the point of contact; $s_{\tau,max}$ is defined as the maximum relative tangential displacement at which particles commence sliding, as defined in Equation (16). η_τ is the tangential damping ratio, which is estimated in Rocky DEM through the following Equation (17):

$$\mu = \begin{cases} \mu_s & \text{if no sliding does occur at the contact interface} \\ \mu_d & \text{if sliding does occur at the contact interface} \end{cases} \tag{15}$$

where μ_s and μ_d represent the static and dynamic friction coefficients, respectively. These parameters can be defined by the user in the corresponding materials interaction editor panel within the Rocky DEM software.

$$s_{\tau,max} = \mu \left(\frac{1 - v_1}{2 - v_1} + \frac{1 - v_2}{2 - v_2} \right)^{-1} s_n \tag{16}$$

where ν_1 and ν_2 represent the Poisson's ratios of the two particles or between a particle and the boundary, contingent upon the specific type of contact.

$$\eta_\tau = -\frac{\ln e}{\sqrt{\ln^2 e + \pi^2}} \tag{17}$$

The Mindlin–Deresiewicz model is exclusively compatible with the Hertzian Spring–Dashpot model. Furthermore, this model exhibits inadequate performance when integrated with any rolling resistance models for non-spherical particles. This limitation stems from a recognized issue that can induce instabilities in the angle of repose. Consequently, when employing the Mindlin–Deresiewicz model in simulations involving non-spherical particles, it is imperative to disable the rolling resistance models within the project [43].

2.6.2. AOR Test Model

The AOR test was conducted using a resin plate positioned beneath a particle inlet (as shown in Figure 9). The particle inlet was precisely aligned directly above the center of the resin plate in accordance with the structural parameters specified by the intelligent powder characteristic tester. To simulate the process of material accumulation, the AOR test was conducted using the fixed funnel method. Seed particles were introduced into the resin plate via free fall from the particle inlet to form a pile. The simulation employed a dynamic particle generation mode. To balance simulation efficiency and result reliability, the generated particles retained their original size. The particle generation rate is established at 0.2 kg/s, with an initial seed mass of 0.2 kg to ensure an adequate number of seeds are introduced into the system. The total simulation duration is set to 3 s to allow sufficient time for excess seeds to exit the domain.

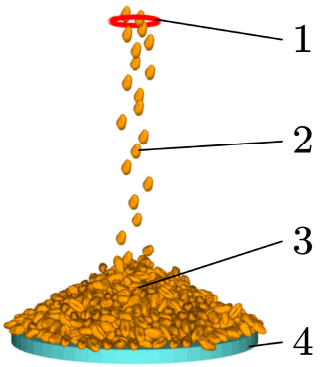
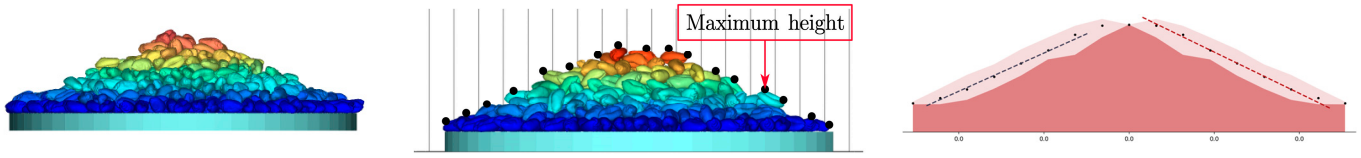


Figure 9. AOR test model: 1. particle inlet; 2. seeds in free fall; 3. stock pile; 4. resin plate.

As illustrated in Figure 10a, the script_calibration_SAOR.py script was imported into the software and activated post-simulation. Multiple cuboid vertical units were automatically generated at the center of the pile to determine the maximum height of particles at the unit's edge (Figure 10b). The vertical element was then rotated by 10° around the pile's vertical axis, and the maximum height of the edge particles was re-extracted. This procedure was repeated 36 times. By calculating the average maximum

height of the particles at the edge of the vertical unit, a regression fitting line was established at the pile's edge, from which the simulation AOR β was derived (Figure 10c).



(**a**) Simulation stop (**b**) Determine the maximum height (**c**) Determination of the AOR

Figure 10. The procedure for determining the AOR.

2.7. Calibration of Simulation Parameters

In this study, the simulation parameters were calibrated through the AOR test model. To identify parameters that significantly influence the AOR, a Plackett–Burman design was employed using Design-Expert software. The minimum and maximum values of the physical experimental parameters were designated as −1 and +1, respectively. A total of nine real parameters (A through I) and two virtual parameters (J and K) were configured in the simulation test. The test design included three central points, resulting in a total of fifteen experimental runs. The simulation test employs the relative error of AOR δ as the evaluation metric, with the calculation formula given as follows:

$$\delta = \frac{|\beta - \alpha|}{\alpha} \times 100\% \tag{18}$$

where δ represents the relative error (%); α denotes the mean value of the actual AOR (°); β signifies the simulation AOR (°).

To narrow the value range of significant parameters following the Plackett–Burman test, a Steepest Ascent test was conducted on the selected significant parameters. Based on the design principles of Box–Behnken and the results from the Plackett–Burman and Steepest Ascent experiments, three levels of significant parameters were identified: high (+1), medium (0), and low (−1). An optimized regression model was constructed using Design-Expert software to establish the relationship between the AOR–significance parameters and the AOR error–significance parameters, thereby determining the optimal combination of these parameters.

2.8. Parameter Optimization and Validation

To establish the optimal parameters of test factors within the given constraint range, a mathematical model for parameter optimization has been developed and validated through AOR testing. The objective of the mathematical model for parameter optimization is to minimize the relative error associated with AOR. The objective function and constraint conditions are detailed in Equation (19).

$$\begin{cases} \min\delta(\mathrm{D},\mathrm{E},\mathrm{H}) \\ \text{s.t.} \begin{cases} 0.15 \leqslant \mathrm{D} \leqslant 0.275 \\ 0.1025 \leqslant \mathrm{E} \leqslant 0.13 \\ 0.07 \leqslant \mathrm{H} \leqslant 0.09 \end{cases} \end{cases} . \tag{19}$$

To further validate the applicability of the wheat seed polyhedron model and its calibration parameters in gas–solid two-phase flow studies, a test bench was established to conduct air-assisted seeding tests. The seeding test bench is illustrated in Figure 11. A high-speed camera (Phantom V9.1, Vision Research, Inc., Wayne, NJ, USA) captures the seeds within the seed tube, while a portable computer stores and processes the captured high-speed footage.

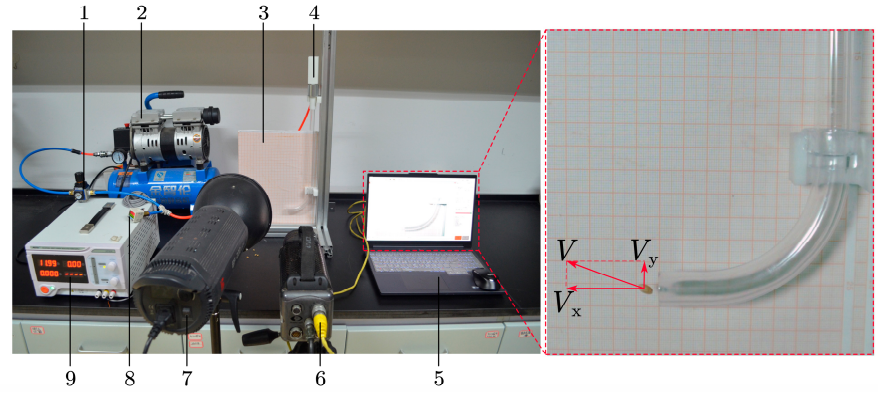


Figure 11. Air-assisted seeding test platform: 1. pressure control valve; 2. air compressor; 3. background panel; 4. seeding device; 5. portable computer; 6. high-speed camera; 7. illumination unit; 8. digital barometer; 9. direct current power supply.

In the bench test, the operating pressure of the seeding device was selected as the test factor, with five levels set at 0, 1, 2, 3, and 4 kPa. The ejection velocity of wheat seeds from the seeding device served as the evaluation index, measured using the Phantom Camera Control 3.9 post-processing software. Each group of bench tests was repeated five times, and the results were averaged. As illustrated in Figure 12, a semi-resolved CFD-DEM coupling simulation model was developed using Fluent and Rocky DEM software to simulate the gas-assisted seeding process of wheat. The fluid domain model was constructed using SpaceClaim 2024R1 software (Figure 12a). This geometry was then imported into Fluent Meshing software, where the grid was divided using the Poly-Hexcore method to achieve joint node connections between structured and unstructured grids (Figure 12b). Transient simulation models for different operating pressures were established in Fluent, and the Case and Data files were subsequently imported into Rocky DEM software. In this study, the Fluent case was configured with a single fluid phase; therefore, the multiphase model was turned off. The viscous model was configured using the standard k-epsilon model (two-equation formulation). The near-wall treatment was configured to utilize scalable wall functions, thereby ensuring accurate representation of turbulence characteristics in the boundary layer. The solution method was configured to utilize Pressure–Velocity Coupling, and the discretization scheme was specified as SIMPLE. Material properties and contact parameters were set based on the aforementioned calibration results. The simulation process is depicted in Figure 12c. The post-processing module was used to extract the ejection velocities of five wheat seeds and calculate their average value.



(**a**) Fluid domain (**b**) Meshing (**c**) Coupling simulation

Figure 12. Semi-resolved CFD-DEM coupling simulation model.

3. Results

3.1. Plackett–Burman Test

The test parameters and results of the Plackett–Burman design are presented in Tables 1 and 2. The data presented in Table 1 are derived from physical experiments. The high (+1) and low (−1) level values of the test factors correspond to the extremum values derived from the data collected through physical experiments. Variance analysis is conducted on the test results, and significant effects are identified using the Lenth method. The findings are summarized in Table 3, and a Pareto chart of standardized factor effects is generated, as illustrated in Figure 13. It is evident that the parameter (H) has a contribution rate of 76.99%, indicating it is a highly significant factor ($p < 0.01$). Additionally, the parameters (D) and (E) have contribution rates of 7.61% and 6.38%, respectively, denoting them as significant factors ($0.01 < p < 0.05$). Parameters (E) and (H) exert negative influences, whereas parameter (D) has a positive effect. Other factors exhibit negligible influence on the relative error of the AOR.

Table 1. Plackett–Burman test parameters.

Symbol	Parameters	Low Level (−1)	High Level (+1)
A	Bulk density of wheat seed $\left(g/cm^3\right)$	0.68	0.79
B	Young′s modulus of wheat seed (MPa)	30.51	90.63
C	Poisson's ratio of wheat seed	0.15	0.46
D	Static friction coefficient of wheat seed	0.15	0.65
E	Dynamic friction coefficient of wheat seed	0.02	0.13
F	Collision restitution coefficient of wheat seed	0.12	0.35
G	Static friction coefficient between wheat seed and resin	0.12	0.55
H	Dynamic friction coefficient between wheat seed and resin	0.01	0.09
I	Collision restitution coefficient between wheat seed and resin	0.31	0.52
J/K	Virtual parameter	/	/

Table 2. Design scheme and results of Plackett–Burman test.

No.	A	B	C	D	E	F	G	H	I	AOR (°)	Relative Error (%)
1	1	1	1	−1	−1	−1	1	−1	1	0.2	99.4
2	−1	1	1	1	−1	−1	−1	1	−1	9.5	71.1
3	1	−1	1	1	1	−1	−1	−1	1	0.3	99.1
4	−1	1	−1	1	1	−1	1	1	1	19.5	40.7
5	1	1	−1	1	1	1	−1	−1	−1	0.4	98.8
6	−1	1	1	−1	1	1	1	−1	−1	1.3	96.1
7	−1	−1	−1	1	−1	1	1	−1	1	0.2	99.4
8	1	1	−1	−1	−1	1	−1	1	1	16.9	48.6
9	0	0	0	0	0	0	0	0	0	8.1	75.4
10	1	−1	1	1	−1	1	1	1	−1	13.8	58.1
11	0	0	0	0	0	0	0	0	0	8.3	74.8
12	0	0	0	0	0	0	0	0	0	8.2	75.1
13	1	−1	−1	−1	1	−1	1	1	−1	24.7	24.9
14	−1	−1	−1	−1	−1	−1	−1	−1	−1	1.6	95.1
15	−1	−1	1	−1	1	1	−1	1	1	34.7	5.5

Table 3. Variance analysis of Plackett–Burman test parameters.

Parameters	Normalization Effect	Mean Sum of Squares	Contribution Rate (%)	F-Value	*p*-Value	Priority Ranking
A	3.5	36.75	0.295	0.5474	0.5005	8
B	12.1	439.23	3.53	6.54	0.0628	4
C	3.63	39.6	0.32	0.5899	0.4853	7
D	16.27	793.81	6.38	11.82	0.0263 *	3
E	−17.77	946.96	7.61	14.1	0.0199 *	2
F	−3.97	47.2	0.38	0.7031	0.4489	6
G	0.067	0.013	0.0001	0.0002	0.9894	9
H	−56.5	9576.75	76.99	142.64	0.0003 **	1
I	−8.57	220.16	1.77	3.28	0.1444	5

Note: An asterisk (*) denotes a significant effect ($0.01 < p < 0.05$), while a double asterisk (**) denotes an extremely significant effect ($p < 0.01$).

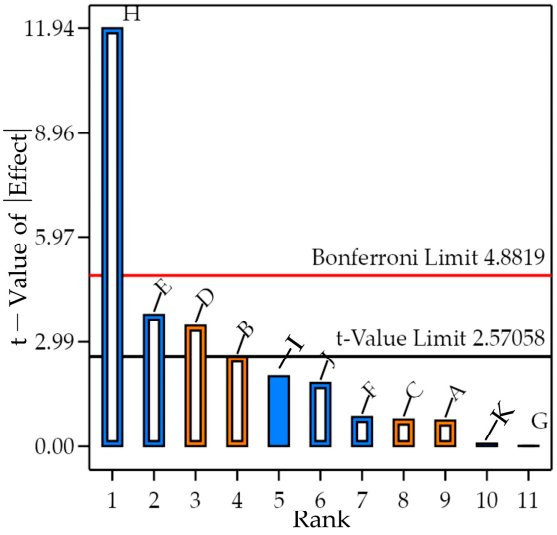


Figure 13. Pareto chart illustrating the normalization effect.

3.2. Steepest Ascent Test

After screening the significant factors based on the Plackett–Burman test results, the Steepest Ascent method was employed to determine the optimal level range of these factors. The direction for steepest ascent was determined according to the positive and negative effects identified in the Plackett–Burman test. Specifically, parameters (E) and (H) exhibit negative effects, while parameter (D) shows a positive effect. Consequently, the steepest ascent experiment was conducted with simultaneous adjustments for parameters (E), (H), and (D). The value range for significant factors was divided into five gradient levels. For non-significant factors, their values were determined by considering the overall effects observed in the Plackett–Burman test. Given that the objective was to optimize the response value towards a minimum, positive effect factors were set at lower levels, whereas negative effect factors were set at higher levels. The simulation test scheme and results are summarized in Table 4. As the wheat–wheat static friction coefficient increased, both the wheat–wheat dynamic friction coefficient and the wheat–resin dynamic friction coefficient decreased, leading to a reduction in the stacking angle and an increase in relative error. Therefore, the high and low levels for the Box–Behnken design were selected from experiments 1 and 2. The optimization ranges for the static friction coefficient of wheat seed, dynamic friction coefficient of wheat seed, and dynamic friction coefficient between wheat seed and resin were set as 0.15–0.275, 0.1025–0.13, and 0.07–0.09, respectively.

Table 4. Design scheme and results of steepest ascent test.

No.	Step Size	D	E	H	AOR(°)	Relative Error (%)
1	0	0.15	0.13	0.09	34.7	5.5
2	0 + 1Δ	0.275	0.1025	0.07	30.3	7.9
3	0 + 2Δ	0.4	0.075	0.05	23.8	27.7
4	0 + 3Δ	0.525	0.0475	0.03	11.0	66.7
5	0 + 4Δ	0.65	0.02	0.01	9.8	70.2

3.3. Box–BehnkenTest

Based on the results of the Plackett–Burman and steepest ascent tests, the optimal range for significant factors was determined. The Box–Behnken design principle was employed, utilizing Design-Expert software for response surface methodology to investigate the influence of parameters (D), (E), and (H) on the relative error δ of the AOR. The coding of test factors is presented in Table 5, while the experimental design and outcomes are detailed in Table 6. A second-order regression model relating the packing angle to experimental factors was established. The variance analysis results for this model are presented in Table 7. The parameter (D), the parameter (E), the quadratic term of the dynamic friction coefficient of wheat seed (E^2), and the quadratic term of the dynamic friction coefficient between wheat seed and resin (H^2) have extremely significant effects on the relative error of the AOR. Additionally, the parameter (H), the interaction term between the static and dynamic friction coefficients of wheat particles (DE), and the interaction term between the static friction coefficient of wheat seed and the dynamic friction coefficient between wheat seed and resin (DH) have significant effects on the relative error of the AOR. The model's *p*-value is 0.0009 ($p < 0.01$), while the *p*-value for the lack-of-fit test is 0.2529 ($p > 0.01$), indicating a good fit. By eliminating insignificant factors, an optimized regression model was obtained, as shown in Equation (20).

$$\delta = 4.75 + 3.59D - 3.16E + 1.95H - 2.75DE + 2.98DH + 6.33E^2 + 6.16H^2 \quad (20)$$

Table 5. Box–Behnken design factor level table.

Coding	Parameters		
	D	E	H
+1	0.275	0.13	0.09
0	0.2125	0.11625	0.08
−1	0.15	0.02	0.07

Table 6. Design scheme and results of Box–Behnken test.

No.	D	E	H	AOR (°)	Relative Error (%)
1	0	−1	−1	27.6	16.1
2	1	1	0	29.7	9.7
3	0	0	0	31.5	4.3
4	−1	0	−1	29.4	10.5
5	1	−1	0	25.7	21.9
6	1	0	−1	29.2	11.3
7	0	0	0	32.1	2.4
8	0	−1	1	25.5	22.5
9	−1	−1	0	30.0	8.8

Table 6. *Cont.*

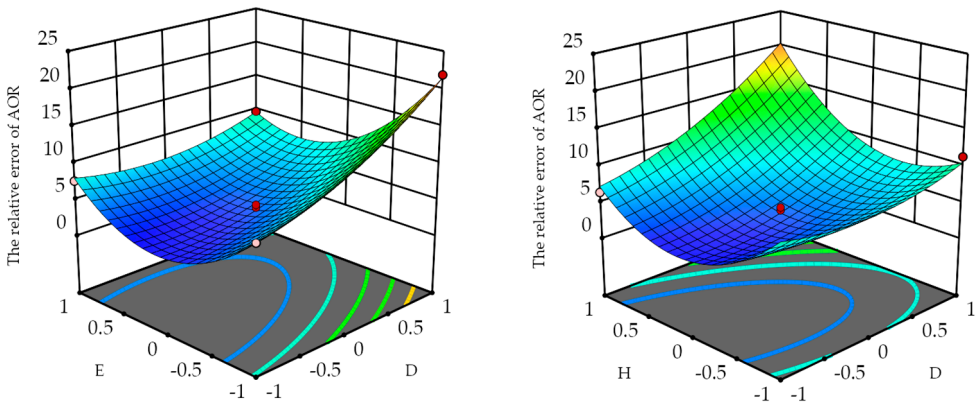
No.	D	E	H	AOR (°)	Relative Error (%)
10	0	1	1	27.6	16.1
11	1	0	1	26.6	19.1
12	0	0	0	31.6	3.9
13	−1	0	1	30.8	6.4
14	−1	1	0	30.4	7.6
15	0	1	−1	36.4	10.6

Table 7. ANOVA of Box–Behnken test.

Sources of Variance	Sum of Squares	Degree of Freedom	Mean Square	F-Value	*p*-Value	
Model	564.08	9	62.68	28.35	0.0009	significant
D	102.96	1	102.96	46.57	0.001 **	
E	80.01	1	80.01	36.19	0.0018 **	
H	30.42	1	30.42	13.76	0.0139 *	
DE	30.25	1	30.25	13.68	0.014 *	
DH	35.4	1	35.4	16.01	0.0103 *	
EH	0.2025	1	0.2025	0.0916	0.7743	
D^2	14.52	1	14.52	6.57	0.0505	
E^2	155.2	1	155.2	70.2	0.0004 **	
H^2	146.94	1	146.94	66.46	0.0005 **	
Residual	11.05	5	2.21			
Lack of fit	9.05	3	3.02	3.01	0.2595	not significant
Pure error	2.01	2	1			
Sum	575.14	14				

Note: An asterisk (*) denotes a significant effect ($0.01 < p < 0.05$), while a double asterisk (**) denotes an extremely significant effect ($p < 0.01$).

The relative error response surface of interaction terms with respect to the AOR is depicted in Figure 14. When parameter (H) is fixed at the 0 level, the interaction response surface between parameters (D) and (E) is illustrated in Figure 14a. At a high level of parameter (E), the relative error of the AOR initially decreases and subsequently increases as parameter (D) increases. Conversely, at a low level of parameter (E), the relative error of the AOR consistently increases with the increase in parameter (D). When parameter (D) is held constant at a small value, the relative error of the AOR first decreases and then increases as parameter (E) increases. When parameter (E) is fixed at the 0 level, the interaction response surface between parameters (D) and (H) is shown in Figure 14b. With parameter (H) fixed, the relative error of the AOR increases as parameter (D) increases. When parameter (D) is fixed, the relative error of the AOR initially decreases and then increases as parameter (H) increases.



(**a**) H = 0 (**b**) E = 0

Figure 14. Response surface of AOR relative error.

3.4. Verification Test

3.4.1. Verification Test of the AOR

The optimal parameter combination was determined through the numerical optimization module of the Design-Expert software. Specifically, the static friction coefficient of wheat seed is 0.15, the dynamic friction coefficient of wheat seed is 0.11694, and the dynamic friction coefficient between wheat seed and resin is 0.0797. These parameters were subsequently input into the simulation software. Verification through simulation testing revealed that the relative error of the corresponding AOR under these optimized parameters was 2.3%. The results indicate that the wheat seed model and the calibrated simulation parameters are reliable.

3.4.2. Semi-Resolved CFD-DEM Coupling Simulation and Verification

The results of the bench and simulation test are presented in Table 8. As the operating pressure of the seeding device increases, the average ejection velocity of wheat seeds also increases. The experimental values are generally lower than the simulated values, but the variation trends in ejection velocity are fundamentally consistent. This discrepancy can be attributed to the fact that the simulation test is conducted under ideal conditions, whereas the bench test is subject to systematic errors. The relative error ranges from a minimum of 1.3% to a maximum of 4.1%, all below 5%, which validates the reliability of the aforementioned calibration parameters.

Table 8. Results of ejection velocity.

Operating Pressure (kPa)	Category	Ejection Velocity (m/s)					Average Value	Relative Error (%)
0	Experimental Value	2.383	2.401	2.321	2.403	2.381	2.378	3.8
	Simulated Value	2.51	2.473	2.398	2.464	2.497	2.468	
1	Experimental Value	2.365	2.415	2.387	2.412	2.395	2.395	4.1
	Simulated Value	2.408	2.369	2.557	2.546	2.579	2.492	
2	Experimental Value	2.472	2.493	2.502	2.485	2.511	2.493	1.3
	Simulated Value	2.483	2.513	2.561	2.588	2.483	2.526	
3	Experimental Value	2.582	2.553	2.498	2.505	2.525	2.533	3.3
	Simulated Value	2.628	2.581	2.588	2.655	2.635	2.617	
4	Experimental Value	2.665	2.652	2.657	2.672	2.636	2.656	2.3
	Simulated Value	2.703	2.721	2.738	2.733	2.697	2.718	

4. Discussion

4.1. Calibration Methodology and Apparatus

In this study, it was determined that the coefficient of dynamic friction between the materials significantly influences the AOR, whereas the coefficient of static friction between the materials was identified as a significant factor in [8–10]. It is important to clarify that the material accumulation method employed in this study differs from the approach described in [8–10]. Those studies employed the hollow cylinder method, wherein at the onset of the experiment, the wheat seeds were in contact with the bottom plate, and the cylinder was subsequently raised at a constant velocity. Consequently, the impact velocity between the seeds and the bottom plate was minimal at the initial moment of contact. In contrast, this study utilized the fixed funnel method, allowing the wheat seed to fall freely from a specified height, resulting in a significantly higher impact velocity upon contact with the bottom plate. Therefore, the difference in impact velocities may account for the discrepancies observed in the conclusions of these studies.

Another study [11] describes the utilization of a rotating drum to measure the dynamic AOR for calibrating material contact parameters. The authors of [12] offer fundamental data on individual and bulk granular material properties specific to wheat seed storage. The calibration methodology and apparatus described in [11,12] are tailored to specific application scenarios, and consequently, a comparative analysis with the findings of this study has not been conducted.

4.2. Discrete Element Method for Particle Modeling

In [13], both single-sphere and multi-sphere models were developed. The findings indicated that the single-sphere model exhibits superior computational efficiency. However, this aspect of computational efficiency was not addressed in the current study. Wheat seeds are classified as concave particles. Further investigation is required to determine if approximating concave particles as convex particles can enhance computational efficiency while maintaining accuracy. The scanning technique was employed to acquire a three-dimensional model of particles in [14–16]. This technique, which has been referenced in this study, has become a standard method for achieving precise particle modeling. The polyhedron model presented in this study can also be utilized for particle breakage research; however, further calibration of the particle breakage model is required. The authors of [17] developed an ellipsoid model. It is important to note that while the ellipsoid model does not fully capture the abdominal groove characteristics of wheat seeds, this limitation highlights the advantage of the polyhedron model in accurately representing such features. The methodology employed for wheat seed size analysis in this paper closely mirrors that described in [18,19]. The triaxial dimensions of wheat seeds exhibited a normal distribution, which is consistent with the conclusions of [18,19]. In comparison, this study possesses certain limitations. Firstly, the research concentrated on a single wheat variety, thereby overlooking the structural characteristic variations among different varieties. Secondly, the impact of coating treatment on material properties was not taken into account.

4.3. Validation Testing Methodology

This study demonstrates that wheat seeds collide with the wall at high velocity during the air-assisted seeding process. Therefore, the calibration method employed in this paper holds significant practical application value. The dynamic and static friction coefficients of wheat seed were identified as significant influencing factors, which is consistent with the conclusions of [8–10]. In the study of gas–solid two-phase flow, the multi-ball bonding model was introduced in [16] and validated through the un-resolved CFD-DEM coupling simulation method. This method necessitates that the particle size be smaller than the mesh size. Theoretically, reducing both the mesh and particle sizes enhances simulation accuracy. This also leads to a proportional increase in computational time. Consequently, it is imperative to strike a balance between mesh size, particle size, simulation accuracy, and computational efficiency. In this study, a semi-resolved CFD-DEM coupling simulation method was employed to validate the calibration parameters. A notable characteristic of this approach is that it allows particle sizes larger than the mesh size. However, more accurate methods such as three-way and four-way coupling were not utilized.

5. Conclusions

The triaxial size, intrinsic parameters, contact parameters and AOR of wheat seeds were measured and analyzed. On this basis, a polyhedron model of wheat seed was developed. The feasibility and validity of the simulation parameters were verified by the comparisons of the simulated results and the experimental results of the static AOR

test based on the fixed funnel method and the airflow-assisted seeding test. The main conclusions in this study are as follows:

(1) The results of the Plackett–Burman test indicate that the static and dynamic friction coefficients of wheat seed have a significant impact on the AOR, whereas dynamic friction coefficient between wheat seed and resin exerts an exceptionally pronounced influence on this parameter.
(2) The results of the Box–Behnken test show the optimized regression model of AOR has good reliability and accuracy. The optimal parameter configuration is as follows: static friction coefficient of wheat particles is 0.15, dynamic friction coefficient of wheat is 0.11694, and the dynamic friction coefficient between wheat and resin is 0.0797. The relative error of the AOR is found to be 2.3%, indicating the errors are small.
(3) The experimental results demonstrate that, although the experimental average ejection velocity is lower than the simulated values, the trends in variation are largely consistent, with a maximum relative error of 4.1%. This suggests that the calibration parameters are robust and suitable for further application in gas–solid two-phase flow studies.
(4) The following challenges and issues warrant attention in future research: Firstly, the geometric variations among different varieties of wheat and the impact of particle size on material fluidity must be considered. Secondly, the three- or four-way CFD-DEM coupling method should be employed to simulate the pneumatic conveying process of wheat seeds. Additionally, the influence of material stacking methods on the AOR should be elucidated.

Author Contributions: Conceptualization, J.H. and C.W.; methodology, L.W.; software, L.W.; validation, H.Y., Z.W. and L.W.; formal analysis, H.Y.; investigation, Z.W.; resources, C.W.; data curation, L.W.; writing—original draft preparation, L.W.; writing—review and editing, L.W.; visualization, L.W.; supervision, C.L.; project administration, Q.W.; funding acquisition, C.W. All authors have read and agreed to the published version of the manuscript.

Funding: This research was funded by the National Natural Science Foundation of China, grant number 52175260 and the Young Scientists Fund of the National Natural Science Foundation of China, grant number 32201674.

Institutional Review Board Statement: Not applicable.

Data Availability Statement: The data presented in this study are available on request from the corresponding author. The data are not publicly available as they are part of ongoing research, and sharing them prematurely could compromise the results or findings.

Acknowledgments: The authors would like to extend sincere gratitude to the National Natural Science Foundation of China for its support.

Conflicts of Interest: The authors declare no conflicts of interest.

Abbreviations

The following abbreviations are used in this manuscript:

CFD	Computational Fluid Dynamics
DEM	Discrete Element Method
AOR	Angle of repose
CT	Computed Tomography
ASG	Automatic Sphere-clump Generator
LY502	Lu Yuan No. 502
L	Length
W	Width

T	Thickness
3D	Three-dimensional

References

1. Zeng, Z.; Ma, X.; Cao, X.; Li, Z.; Wang, X. Critical Review of Applications of Discrete Element Method in Agricultural Engineering. *Trans. Chin. Soc. Agric. Mach.* **2021**, *52*, 1–20. [CrossRef]
2. Ma, S.; Xu, L.; Yuan, Q.; Niu, C.; Zeng, J.; Chen, C.; Wang, S.; Yuan, X. Calibration of discrete element simulation parameters of grapevine antifreezing soil and its interaction with soil-cleaning components. *Trans. Chin. Soc. Agric. Eng.* **2020**, *36*, 40–49. [CrossRef]
3. Yu, Q.; Liu, Y.; Chen, X.; Sun, K.; Lai, Q. Calibration and Experiment of Simulation Parameters for Panax notoginseng Seeds Based on DEM. *Trans. Chin. Soc. Agric. Mach.* **2020**, *51*, 123–132. [CrossRef]
4. Al-Hashemi, H.M.B.; Al-Amoudi, O.S.B. A review on the angle of repose of granular materials. *Powder Technol.* **2018**, *330*, 397–417. [CrossRef]
5. Ma, W.; You, Y.; Wang, D.; Yin, S.; Huan, X. Parameter Calibration of Alfalfa Seed Discrete Element Model Based on RSM and NSGA-II. *Trans. Chin. Soc. Agric. Mach.* **2020**, *51*, 136–144. [CrossRef]
6. Wu, M.; Cong, J.; Yan, Q.; Zhu, T.; Peng, X.; Wang, Y. Calibration and experiments for discrete element simulation parameters of peanut seed particles. *Trans. CSAE* **2020**, *36*, 30–38. [CrossRef]
7. Liu, F.; Zhang, J.; Chen, J. Construction of visco-elasto-plasticity contact model of vibratory screening and its parameters calibration for wheat. *Trans. CSAE* **2018**, *34*, 37–43. [CrossRef]
8. Liu, F.; Zhang, J.; Li, B.; Chen, J. Calibration of parameters of wheat required in discrete element method simulation based on repose angle of particle heap. *Trans. CSAE* **2016**, *32*, 247–253. [CrossRef]
9. Zhang, W.; Wu, W.; Lyu, S.; Wang, X.; Jia, H.; Liu, P.; Hou, N.; Zhao, Q. Experimental calibration of wheat mechanical parameters and contact parameters in milling. *J. Henan Univ. Technol.* **2023**, *44*, 105–112. [CrossRef]
10. Wang, X.F.; Wu, W.B.; Jia, H.P. Calibration of discrete element parameters for simulating wheat crushing. *Food Sci. Nutr.* **2023**, *11*, 7751–7764. [CrossRef]
11. Sugirbay, A.; Hu, G.R.; Chen, J.; Mustafin, Z.; Muratkhan, M.; Iskakov, R.; Chen, Y.; Zhang, S.; Bu, L.X.; Dulatbay, Y.; et al. A Study on the Calibration of Wheat Seed Interaction Properties Based on the Discrete Element Method. *Agriculture* **2022**, *12*, 1497. [CrossRef]
12. Horabik, J.; Wiacek, J.; Parafiniuk, P.; Banda, M.; Kobylka, R.; Stasiak, M.; Molenda, M. Calibration of discrete-element-method model parameters of bulk wheat for storage. *Biosyst. Eng.* **2020**, *200*, 298–314. [CrossRef]
13. Petingco, M.C.; Casada, M.E.; Maghirang, R.G.; Thompson, S.A.; Turner, A.P.; McNeill, S.G.; Montross, M. Discrete element method simulation of wheat bulk density as affected by grain drop height and kernel size distribution. *J. Asabe* **2022**, *65*, 555–566. [CrossRef]
14. Zhou, Y.; Shang, W.Y.; Hui, Y.B.; Shi, C.; Gao, J.; Zhang, Y.Z.; Liu, J.J.; Cheng, D.D.; Zhu, K. Construction of an Accurate Wheat-Grain Model Based on X-ray Tomography and Bonding Parameters by Discrete Element. *Appl. Sci.* **2023**, *13*, 9265. [CrossRef]
15. Chen, Z.P.; Wassgren, C.; Veikle, E.; Ambrose, K. Determination of material and interaction properties of maize and wheat kernels for DEM simulation. *Biosyst. Eng.* **2020**, *195*, 208–226. [CrossRef]
16. Ma, D.X.; Shi, S.; Hou, J.L.; Zhou, J.L.; Li, H.; Li, J.F. Calibration and Experimentation of Discrete Elemental Model Parameters for Wheat Seeds with Different Filled Particle Radii. *Appl. Sci.* **2024**, *14*, 2075. [CrossRef]
17. Lu, C.Y.; Gao, Z.; Li, H.W.; He, J.; Wang, Q.J.; Wei, X.Y.; Wang, X.H.; Jiang, S.; Xu, J.; He, D.; et al. An ellipsoid modelling method for discrete element simulation of wheat seeds. *Biosyst. Eng.* **2023**, *226*, 1–15. [CrossRef]
18. Sun, K.; Yu, J.Q.; Liang, L.S.; Wang, Y.; Yan, D.X.; Zhou, L.; Yu, Y.J. A DEM-based general modelling method and experimental verification for wheat seeds. *Powder Technol.* **2022**, *401*, 22. [CrossRef]
19. Fan, J.H.; Wang, H.W.; Sun, K.; Zhang, L.; Wang, L.; Zhao, J.W.; Yu, J.Q. Experimental verification and simulation analysis of a multi-sphere modelling approach for wheat seed particles based on the discrete element method. *Biosyst. Eng.* **2024**, *245*, 135–151. [CrossRef]
20. Gao, W.; Feng, Y.; Wang, C.Y. A coupled isogeometric/multi-sphere discrete element approach for the contact interaction between irregular particles and structures. *Powder Technol.* **2023**, *430*, 12. [CrossRef]
21. Zhong, W.Q.; Yu, A.B.; Liu, X.J.; Tong, Z.B.; Zhang, H. DEM/CFD-DEM Modelling of Non-spherical Particulate Systems: Theoretical Developments and Applications. *Powder Technol.* **2016**, *302*, 108–152. [CrossRef]
22. Zhang, R.; Zhou, J.; Liu, H.; Shi, S.; Wei, G.; He, T. Determination of Interspecific Contact Parameters of Corn and Simulation Calibration of Discrete Element. *Trans. Chin. Soc. Agric. Mach.* **2022**, *53*, 69–77. [CrossRef]

23. Shi, Q.; Sakai, M. Recent progress on the discrete element method simulations for powder transport systems: A review. *Adv. Powder Technol.* **2022**, *33*, 23. [CrossRef]
24. Ma, H.Q.; Zhou, L.Y.; Liu, Z.H.; Chen, M.Y.; Xia, X.H.; Zhao, Y.Z. A review of recent development for the CFD-DEM investigations of non-spherical particles. *Powder Technol.* **2022**, *412*, 62. [CrossRef]
25. Zhang, C.; Liu, T.; Zheng, Z.; Fang, J.; Xie, X.; Chen, L. Design and test of the precision seeding dispenser with the staggered convex teeth for wheat sowing with wide seedling belt. *Trans. CSAE* **2024**, *40*, 47–59. [CrossRef]
26. Yu, C.; Chen, Z.; Chen, L. Design and Test of Electronic Control Seeding System for Wheat Plot Drill. *Trans. Chin. Soc. Agric. Mach.* **2023**, *54*, 75–83. [CrossRef]
27. Hou, J.; Ma, D.; Li, H.; Zhang, Z.; Zhou, J.; Shi, S. Design and Experiment of Pneumatic Centrifugal Combined Precision Seed Metering Device for Wheat. *Trans. Chin. Soc. Agric. Mach.* **2023**, *54*, 35–45. [CrossRef]
28. Amjad, W.; Chen, Z.; Ambrose, K. Design assessment of grain inverters in cross-flow grain dryer via CFD-DEM numerical simulation. *Biosyst. Eng.* **2024**, *239*, 147–157. [CrossRef]
29. Wang, L.; Yang, H.; Wang, Q.; Lu, C.; Wang, C.; He, J. Design and Experiment of Air-assisted Linear Seeding Device for Wheat. *Trans. Chin. Soc. Agric. Mach.* **2024**, *55*, 111–120. [CrossRef]
30. Wang, C.; Li, H.W.; He, J.; Wang, Q.J.; Lu, C.Y.; Yang, H.Y. Optimization Design of a Pneumatic Wheat-Shooting Device Based on Numerical Simulation and Field Test in Rice-Wheat Rotation Areas. *Agriculture* **2022**, *12*, 56. [CrossRef]
31. Xu, D.; Li, Y.; Xu, X.; Zhang, Y.; Yang, L. Numerical Study of Wheat Particle Flow Characteristics in a Horizontal Curved Pipe. *Processes* **2024**, *12*, 900. [CrossRef]
32. Dai, F.; Song, X.F.; Zhao, W.Y.; Han, Z.S.; Zhang, F.W.; Zhang, S.L. Motion simulation and test on threshed grains in tapered threshing and transmission device for plot wheat breeding based on CFD-DEM. *Int. J. Agric. Biol. Eng.* **2019**, *12*, 66–73. [CrossRef]
33. Dai, F.; Song, X.F.; Shi, R.J.; Guo, W.J.; Zhao, Y.M.; Wang, F.; Zhao, W.Y. Movement law of the threshing material in threshing and cleaning machine for plot-bred wheat. *Int. J. Agric. Biol. Eng.* **2022**, *15*, 100–106. [CrossRef]
34. Liu, Y.; Mi, G.P.; Zhang, S.L.; Li, P.; Huang, Y.X. Determination of Discrete Element Modelling Parameters of Adzuki Bean Seeds. *Agriculture* **2022**, *12*, 626. [CrossRef]
35. Li, G.; Li, H.; Li, X.; Gong, Z.; Yang, Q.; Huang, Y.; Fu, Z. Establishment and Calibration of Discrete Element Model for Buckwheat Seed Based on Static and Dynamic Verification Test. *Agriculture* **2023**, *13*, 1024. [CrossRef]
36. Ren, D.-Z.; Zhang, L.-J.; Gong, Y.-J.; Meng, J.; He, T.-Y. Calibration and Testing of Discrete Element Model Parameters for Biochar-based Fertilizer. *J. Shenyang Agric. Univ.* **2023**, *54*, 447–455.
37. Malone, K.F.; Xu, B.H. Determination of contact parameters for discrete element method simulations of granular systems. *Particuology* **2008**, *6*, 521–528. [CrossRef]
38. Chen, J.; Tian, T.; Li, J.; You, Z. Effects of operating parameters and particle friction on water usage of deep-sea manganese nodules hydraulic conveying equipment. *Powder Technol.* **2024**, *442*, 119850. [CrossRef]
39. Tsuji, Y.; Tanaka, T.; Ishida, T. Lagrangian numerical-simulation of plug flow of cohesionless particles in a horizontal pipe. *Powder Technol.* **1992**, *71*, 239–250. [CrossRef]
40. Antypov, D.; Elliott, J.A. On an analytical solution for the damped Hertzian spring. *Europhys. Lett.* **2011**, *94*, 6. [CrossRef]
41. Zhang, C.; Guo, S.; Shang, F.; Ge, Z.; Guo, L. Numerical simulation of particle jet in supercritical water environment based on an improved coarse-grained CFD-DEM method. *Powder Technol.* **2025**, *456*, 120833. [CrossRef]
42. Petit, H.A.; Potapov, A.V.; Tavares, L.M. Simulating breakage by compression of iron ore pellets using the discrete breakage model. *Powder Technol.* **2025**, *449*, 120433. [CrossRef]
43. Ansys® Rocky. *Release 2024 R1, Help System, Rocky Technical Manual*; Ansys, Inc.: Canonsburg, PA, USA, 2024.

Disclaimer/Publisher's Note: The statements, opinions and data contained in all publications are solely those of the individual author(s) and contributor(s) and not of MDPI and/or the editor(s). MDPI and/or the editor(s) disclaim responsibility for any injury to people or property resulting from any ideas, methods, instructions or products referred to in the content.